

• Original Paper •

Aerosol Optical Properties and Radiative Impacts in the Pearl River Delta Region of China during the Dry Season

Boru MAI¹, Xuejiao DENG¹, Zhanqing LI^{*2,3}, Jianjun LIU³, Xiang'ao XIA^{4,5},
Huizheng CHE⁶, Xia LIU⁷, Fei LI¹, Yu ZOU¹, and Maureen CRIBB³

¹*Institute of Tropical and Marine Meteorology, China Meteorological Administration, Guangzhou 510640, China*

²*State Key Laboratory of Earth Surface Processes and Resource Ecology and College of Global Change and Earth System Science, Beijing Normal University, Beijing 100875, China*

³*Earth System Science Interdisciplinary Center and Department of Atmospheric and Oceanic Science, University of Maryland, College Park, Maryland MD 20740 USA*

⁴*Laboratory for Middle Atmosphere and Global Environment Observation, Institute of Atmospheric Physics, Chinese Academy of Sciences, Beijing 100029, China*

⁵*School of Earth Sciences, University of Chinese Academy of Sciences, Beijing 100049, China*

⁶*Chinese Academy of Meteorological Sciences, Beijing 100081, China*

⁷*Guangzhou Meteorological Observatory, Guangzhou 511430, China*

(Received 12 April 2017; revised 17 August 2017; accepted 26 September 2017)

ABSTRACT

Aerosol optical properties and direct radiative effects on surface irradiance were examined using seven years (2006–2012) of Cimel sunphotometer data collected at Panyu—the main atmospheric composition monitoring station in the Pearl River Delta (PRD) region of China. During the dry season (October to February), mean values of the aerosol optical depth (AOD) at 550 nm, the Ångström exponent, and the single scattering albedo at 440 nm (SSA) were 0.54, 1.33 and 0.87, respectively. About 90% of aerosols were dominated by fine-mode strongly absorbing particles. The size distribution was bimodal, with fine-mode particles dominating. The fine mode showed a peak at a radius of 0.12 μm in February and October ($\sim 0.10 \mu\text{m}^3 \mu\text{m}^{-2}$). The mean diurnal shortwave direct radiative forcing at the surface, inside the atmosphere (F_{ATM}), and at the top of the atmosphere, was -33.4 ± 7.0 , 26.1 ± 5.6 and $-7.3 \pm 2.7 \text{ W m}^{-2}$, respectively. The corresponding mean values of aerosol direct shortwave radiative forcing per AOD were -60.0 ± 7.8 , 47.3 ± 8.3 and $-12.8 \pm 3.1 \text{ W m}^{-2}$, respectively. Moreover, during the study period, F_{ATM} showed a significant decreasing trend ($p < 0.01$) and SSA increased from 0.87 in 2006 to 0.91 in 2012, suggesting a decreasing trend of absorbing particles being released into the atmosphere. Optical properties and radiative impacts of the absorbing particles can be used to improve the accuracy of inversion algorithms for satellite-based aerosol retrievals in the PRD region and to better constrain the climate effect of aerosols in climate models.

Key words: aerosol properties, radiative forcing, Pearl River Delta region, dry season

Citation: Mai, B. R., and Coauthors, 2018: Aerosol optical properties and radiative impacts in the Pearl River Delta region of China during the dry season. *Adv. Atmos. Sci.*, **35**(2), 195–208, <https://doi.org/10.1007/s00376-017-7092-4>.

1. Introduction

Aerosols are recognized as a major factor in determining global and regional climate changes (Ramanathan et al., 2001; IPCC, 2013; Li et al., 2016). They play crucial roles not only in radiative transfer in the atmosphere (Kosmopoulos et al., 2008), but also in the hydrological cycle (Rosenfeld et al., 2008; Clarke and Kapustin, 2010), the carbon cycle (Chameides et al., 1999), and some important environmental

issues such as acid rain and tropospheric ozone pollution (Wang, 1999). To date, the consideration of aerosol effects in climate models is still limited (Anderson et al., 2003), mainly because of the diversity in their source and composition, and varying trends in aerosol loading as well as the non-uniform distribution of radiative forcing (IPCC, 2013). Therefore, the understanding of the impacts of aerosols on the environment and climate is largely dependent on investigating the spatiotemporal distributions of the particles and on the accurately calculating their optical and radiative properties.

Ground-based remote sensing observations provide reliable and continuous column-integrated aerosol optical and ra-

* Corresponding author: Zhanqing LI
Email: zli@atmos.umd.edu

diative properties for validating satellite-based measurements and model simulations. To date, several ground-based aerosol observation networks have been established: the Aerosol Robotic Network (AERONET; Holben et al., 1998), AERosol CANada (Bokoye et al., 2001); the Sky Radiometer Network (Nakajima et al., 2003); the Aerosol Ground Station Network (Mitchell and Forgan, 2003); the Chinese Sun Hazemeter Network (Xin et al., 2007); and the China Aerosol Remote Sensing Network (CARSNET; Che et al., 2009a, 2015). The latter two of these networks are operated by the Institute of Atmospheric Physics using portable LED hazemeters and by the China Meteorological Administration using CE-318 sunphotometers, respectively. These networks provide ground-based measurements of aerosol loading and properties for the assessment of satellite retrievals (Li et al., 2007), for evaluations of the aerosol direct radiative effect in China (Li et al., 2010), and for validations of regional climate and environment models (Zhuang et al., 2013).

Aerosol optical depth (AOD), the Ångström exponent (AE), and the single scattering albedo (SSA) are basic aerosol optical parameters for determining the radiative and climatic effects of anthropogenic and natural aerosol particles. Previous studies using these parameters have shown that aerosols in China have little impact on the atmosphere–surface system, but substantially warm up the atmosphere at the expense of cooling the surface (Li et al., 2010). The magnitudes of aerosol radiative effects are closely correlated with aerosol source, type, and absorption (Koren et al., 2004; Qin and Mitchell, 2009; Xia et al., 2016). Absorbing aerosols, such as soot, modify the vertical distribution of heating rates and therefore change the stability of the atmosphere (Ackerman et al., 2000; Koren et al., 2004). Many field campaigns examining aerosol properties and radiative effects in different aerosol source regions have been carried out in recent years (Li et al., 2010; Liu et al., 2011; Xin et al., 2014). These studies have mainly focused on relatively rural regions for better representation of background conditions in China (Che et al., 2009b; Wang et al., 2010), as well as in northern, eastern and southeastern China where aerosols are composed of dust and anthropogenic aerosols (Xia et al., 2007a; Liu et al., 2012; Wang et al., 2014). To date, however, an assessment of the aerosol impact on radiative transfer is still lacking in the strong aerosol source region of the Pearl River Delta (PRD). This assessment is needed because this region is dominated by carbonaceous aerosols such as soot and organic aerosols (Wu et al., 2009; Cao et al., 2003, 2004), which have reduced by more than half the surface radiation, especially at ultraviolet wavelengths (Deng et al., 2011). Moreover, aerosols in this region substantially delay precipitation and lightning (Guo et al., 2016).

Since 2006, extensive measurements of aerosol optical, physical, and chemical properties have been made at Panyu (23°N, 113.35°E; 141 m above sea level), which offer a long-term data source to investigate regional climate change related to aerosol variations in China. The site is located in the heart of the PRD region and is surrounded by several large cities: Guangzhou to the south; Dongguan to the west; and

Shenzhen and Hong Kong to the northwest (Fig. 1). In 2011, Panyu became the first CARSNET site in the PRD region. Measurements made at Panyu represent the basic compositional characteristics of the atmosphere in the PRD region (Wu et al., 2009).

In this study, seven years (2006–2012) of sunphotometer data from this region were examined for the first time. The aims of the work were to: (1) analyze the frequency and monthly distributions of AOD, SSA, AE, and relative humidity (RH); (2) classify major aerosol types using the AE, the co-SSA (ω), and volume size distributions; and (3) examine the aerosol direct radiative forcing (ADRF) and forcing efficiency (FE) over the region. Section 2 describes the instrumentation at the site and the methodology used in the study. Section 3 presents the results and discussion. Conclusions are given in section 4.

2. Data and methodology

2.1. Instrumentation

The characterization of atmospheric aerosols was performed using a sunphotometer (Cimel Électronique, Paris, France). This instrument measures direct solar radiation every 15 min with a 1.2° full field-of-view at 1020, 870P1, 670, 440, 870P2, 870, 936, and 870P3 nm (P indicates a polarized filter). The full-width at half-maximum of each interference filter is 10 nm. Measurements at 1020, 870, 670, and 440 nm are used to retrieve AOD. The raw AOD is cloud-screened according to the method of Smirnov et al. (2000), with an uncertainty of $< \pm 0.01$ for wavelengths > 440 nm (Eck et al., 1999).

The Cimel sunphotometer also measures sky radiances under almucantar and principal plane scenarios at 440, 670, 870 and 1020 nm following the optical air mass protocol described by Holben et al. (1998). Aerosol inversion algorithms and software (SKYRAD.pack version 4.2) are used to retrieve aerosol optical and microphysical properties from sky radiances. Other aerosol characteristics, such as SSA, the

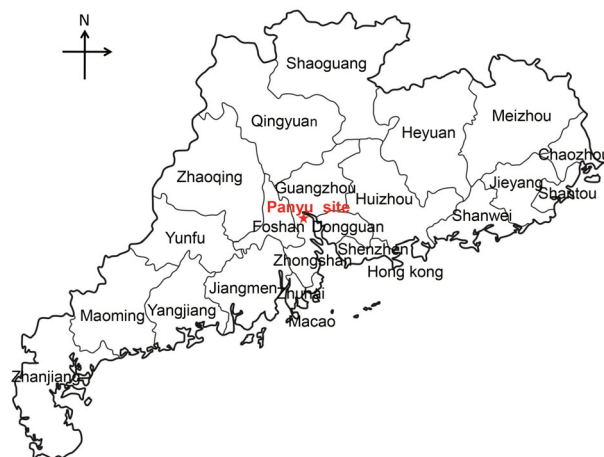


Fig. 1. Location of Panyu—the observation site in the PRD region.

refractive index, and the particle volume size distribution, are obtained by this technique (Nakajima et al., 1996). Calibration of the sunphotometer was performed by CARSNET following the protocol developed by AERONET. Details about the intercomparison calibration and sphere calibration carried out at the Chinese Academy of Meteorological Sciences are given in Che et al. (2009a) and Tao et al. (2014).

2.2. Methodology

2.2.1. Retrievals of AOD, ω , and AE

The retrieval of columnar aerosol optical properties from sky radiances requires an accurate correction for the effects of multiple scattering and for the contribution of light reflected from the earth's surface and scattered downward in the atmosphere (Valenzuela et al., 2012). The SKYRAD.pack version 4.2 software (Nakajima et al., 1996), which is commonly used to retrieve aerosol optical and radiative parameters (e.g., Kim et al., 2005; Che et al., 2008; Liu et al., 2008; Khatri et al., 2014; Wang et al., 2014), was used to calculate the AOD and SSA by using linear and nonlinear inversion schemes developed based on radiative transfer calculations. Additional input parameters for the SKYRAD.pack software include the Moderate Resolution Imaging Spectroradiometer (MODIS) Level 2 Collection 5 total ozone amount product (MOD07, 5 km \times 5 km, daily) and the spectral surface reflectance product at seven wavelengths (MOD09, 0.5 km \times 0.5 km, every eight days). The SSA is typically used to characterize aerosol absorption and is a key variable in assessing the radiative forcing due to aerosols. The ω describes the loss of photons to absorption, which is useful in identifying particle composition, especially carbonaceous particles (Corrigan et al., 2006). Here, ω is expressed as

$$\omega(\lambda) = 1 - \text{SSA}(\lambda), \quad (1)$$

where λ is the wavelength.

The AE is a good indicator of particle size and is given by the following equation:

$$\text{AE} = -\frac{\ln\left[\frac{\text{AOD}(\lambda_1)}{\text{AOD}(\lambda_2)}\right]}{\ln\left(\frac{\lambda_1}{\lambda_2}\right)}, \quad (2)$$

where λ_1 and λ_2 are the two wavelengths chosen to calculate the AE. The wavelength pairing of 440 nm and 870 nm was used in this study. The AE can range from negative values to greater than 1 (Gobbi et al., 2007), depending on the particle size.

2.2.2. Radiative forcing and radiative forcing efficiency

Radiative fluxes and aerosol direct radiative effects of total, diffuse, and direct shortwave irradiances in the broadband spectral range (0.25–4.00 μm) were calculated using the Santa Barbara Discrete Ordinate Radiative Transfer Model (DISORT) Atmospheric Radiative Transfer (SBDART) model (Ricchiazzi et al., 1998). The SBDART model is based on low-resolution band models developed for LOWTRAN 7 atmospheric transmission and the DISORT radiative transfer model, which has 33 layers and four radiation

streams. Various studies have shown that the SBDART model can successfully simulate downwelling broadband fluxes at the surface and upwelling fluxes at the top of the atmosphere (TOA; Xia et al., 2007a; Li et al., 2010). SBDART simulations and measurements of broadband irradiance agree to within 3% (Halthore et al., 2005). This model has been used to estimate aerosol radiation forcing in China (Liu et al., 2007; Xia et al., 2007c, 2007d; Li et al., 2010).

The AOD, SSA, AE, and Asymmetry factor (ASY) at four AERONET wavelengths (i.e., 440, 675, 870, and 1020 nm) have been used to interpolate and extrapolate into the spectral divisions of the SBDART model (Xia et al., 2007a, 2007b). Values for the ASY ($\text{ASY}_{440\text{ nm}} = 0.73$; $\text{ASY}_{675\text{ nm}} = 0.66$, $\text{ASY}_{870\text{ nm}} = 0.63$; $\text{ASY}_{1020\text{ nm}} = 0.61$) from the AERONET site in Hong Kong (about 110 km to the southeast of Panyu) were used in this study and assumed to be constant. Vertical profiles of water vapor and ozone were obtained by partitioning total column water vapor amounts and total ozone amounts from the MOD07 product according to a standard model atmosphere (McClatchey et al., 1972). The surface albedo from the MODIS Albedo product (MCD43B3, https://lpdaac.usgs.gov/dataset_discovery/modis/modis_products_table/mcd43b3) was derived using the 16-day anisotropy model provided in the MODIS BRDF/Albedo Model Parameters product (MCD43B1) at a resolution of 500 m. The total shortwave broadband albedo was used according to algorithms developed by Liang (2001) and set to be constant within the retrieval period.

ADRF denotes the direct effect of aerosols on the atmospheric energy budget. The SBDART model was run twice to simulate shortwave irradiances with and without aerosol particles under cloud-free conditions, and then used to determine the ADRF at the surface (F_{SFC}) and at the TOA (F_{TOA}). The aerosol radiative forcing within the atmosphere (F_{ATM}) was defined as the difference between F_{TOA} and F_{SFC} . Instantaneous values of ADRF at different levels were calculated using the following equations:

$$\Delta F = F \downarrow - F \uparrow, \quad (3)$$

$$F_{\text{TOA}} = \Delta F_{\text{TOA, with_aerosol}} - \Delta F_{\text{TOA, without_aerosol}}, \quad (4)$$

$$F_{\text{SFC}} = \Delta F_{\text{SFC, with_aerosol}} - \Delta F_{\text{SFC, without_aerosol}}, \quad (5)$$

$$F_{\text{ATM}} = F_{\text{TOA}} - F_{\text{SFC}}, \quad (6)$$

where ΔF denotes the net downward flux (downward radiation, $F \downarrow$, minus upward radiation, $F \uparrow$).

The diurnal mean radiative forcing is given as

$$dF = \frac{1}{24} \int F(t) dt, \quad (7)$$

where t is the definite integral of time over the whole day or daytime only, and $F(t)$ represents instantaneous radiative forcing values. On a given day, the number of data points may be limited because of the presence of clouds. To alleviate this limitation, monthly mean values from all instantaneous measurements were determined, from which monthly and annual means of shortwave ADRF were computed (Kim et al., 2005; Li et al., 2010). The uncertainties in the main input parameters of AOD, AE, SSA, ASY, surface reflectance,

and ozone amounts caused an error of $8.76 \pm 3.44 \text{ W m}^{-2}$ (Li et al., 2010).

We also computed the FE, defined as the change in diurnal mean radiative forcing (F) with respect to the change in AOD at 550 nm:

$$FE = \frac{F}{AOD(\lambda_{550})} \quad (8)$$

λ_{550} was the wavelength at 550 nm. FE was calculated at the surface (FE_{SFC}), at the TOA (FE_{TOA}), and within the atmosphere (FE_{ATM}) using Eqs. (3)–(8) (Li et al., 2010; Liu et al., 2011). The units are W m^{-2} for ADRF and W m^{-2} per AOD for FE. The AOD was calculated by the following equation (Ångström, 1964):

$$AOD(\lambda) = \beta \lambda^{-AE} \quad (9)$$

where λ is the wavelength (here, 550 nm) and β is the turbidity coefficient (AOD at $\lambda = 1 \mu\text{m}$).

2.2.3. Data

Data derived from the sky radiation algorithm were used to analyze the AOD, SSA and AE at a temporal resolution of 30 min. The temporal resolution of ADRF was the same as that of the aerosol property parameters. There were 1219 measurements acquired by the sunphotometer from January 2006 to December 2012. However, observations were not continuous because of instrument calibration and maintenance (Zhu et al., 2014). In addition, the PRD region is typically cloudy and rainy during the wet seasons (spring and summer), which greatly influences instrument observations and data inversions. For this reason, this study focused on the dry season (October through February).

3. Results and discussion

3.1. Aerosol optical properties

Figure 2a shows the frequency distribution of AOD at 550 nm for each month. The number of samples in each month (October, November, December, January, and February) was 109, 273, 373, 357 and 107, respectively. In general, the pattern in the frequency of AOD followed a Gaussian distribution, which is in accordance with Behnert et al. (2007) but different from the log-normal distribution reported by Liu et al. (2008). The AOD ranged from ~ 0.1 – 1.5 , with more instances of high AOD in October and February than in other months. The frequencies of occurrence of AOD < 0.3 were 7.4% (October), 9.5% (November), 23.9% (December), 5.3% (January), and 0.00% (February). The frequencies of occurrence of AOD > 0.7 were 40.74% (October), 20.9% (November), 19.0% (December), 13.2% (January), and 56.1% (February). The frequencies of occurrence of AOD between 0.3 and 0.7 were 51.9%, 69.6%, 57.1%, 81.5% and 43.9%, respectively. This indicates that high AOD prevails during the dry season of the PRD region. About 11.7% of all AOD values were less than 0.2, with the greatest

proportion of these values occurring in February. A greater proportion of AOD values less than 0.2 (22%) has been reported at Xianghe, where frequent airflow outbreaks lead to a relatively higher occurrence of background aerosol loading levels (Xia et al., 2005, 2007c). The low AOD situation in the PRD region most likely arises from the wet scavenging of aerosols after precipitation. However, these events are typically short-lived because of the high RH conditions prevalent in the region, in addition to the presence of local aerosol sources (Wang et al., 2014).

Figure 2b shows the monthly variability in AOD at different wavelengths. The first and second highest monthly mean values of AOD occurred in February and October (0.9 and 0.7, respectively). The minimum monthly mean value of AOD (0.5) occurred in December. Note that the monthly mean AODs from November to January were not significantly different ($p > 0.05$). The magnitudes of AODs from October to February were similar to those measured in Hefei, where the AOD is influenced by temperature, RH via hygroscopic growth, and stagnant weather conditions (Wang et al., 2014). The air temperature is of significance for the vertical convection of the aerosol loading. Considering that the temperature in February over the PRD region is relatively low

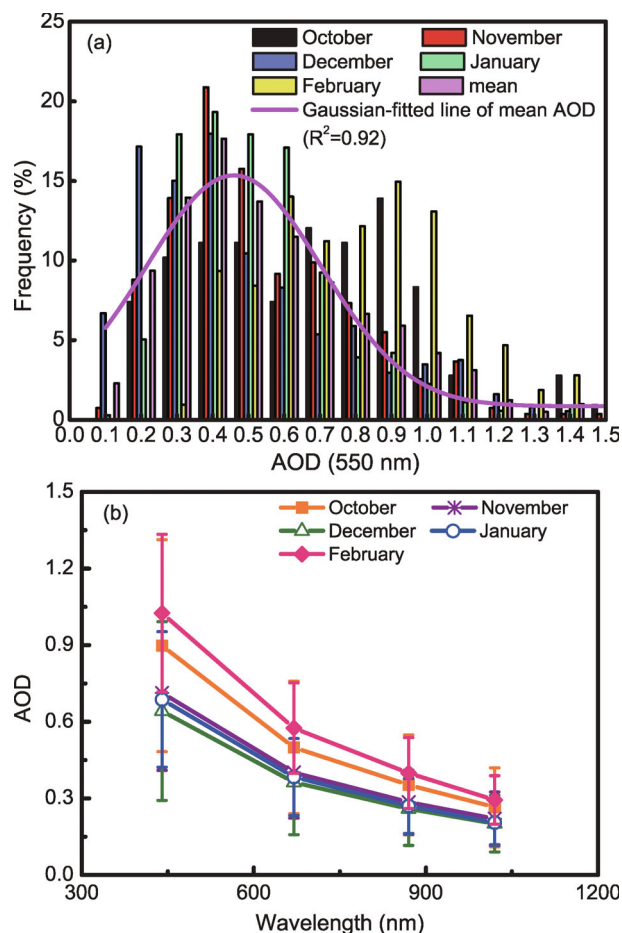


Fig. 2. (a) Frequency distributions of AOD at 500 nm and (b) monthly variations in AOD at different wavelengths in the PRD region.

compared to the other months, the maximum AOD value occurring in February is most likely due to the presence of frequent stagnant weather systems and the swelling effect caused by high RH.

The SSA mainly depends on the chemical composition and size distribution of aerosol particles (Wang et al., 2014). Figure 3a shows the frequency of occurrence of SSA at 440 nm. The histograms of SSA have a Gaussian distribution. The frequencies of occurrence in October and February were higher than in other months. The frequencies of occurrence of SSA values < 0.8, > 0.92, and from 0.8 to 0.92, were 7.6%, 84.8%, and 14.3%, respectively. This suggests that the aerosols were strongly absorbing.

Relatively high values of SSA were seen in October (0.90 ± 0.04), followed by moderate values in February (0.88 ± 0.05) and lower values in the other months (ranging from 0.86 ± 0.05 to 0.87 ± 0.053) (Fig. 3b). The mean value of SSA was 0.87, which is lower than that reported at Xianghe (39.753°N , 116.961°E), a site located between two megacities (Beijing 70 km to the northwest and Tianjin 70 km to

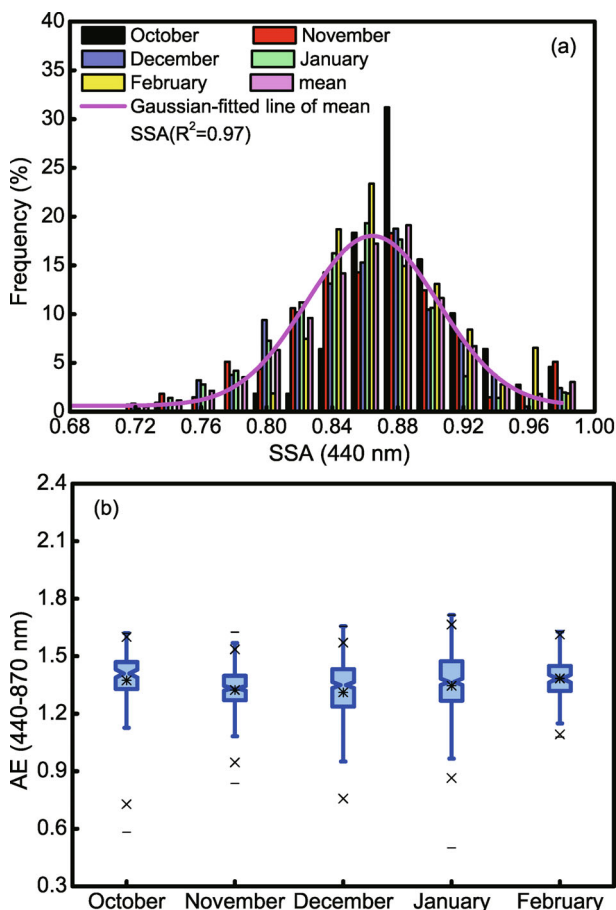


Fig. 3. (a) Frequency distributions of SSA at 440 nm and (b) monthly variations in SSA at 440 nm in the PRD region. The notches in the notched box and whisker plots represent the 95% confidence levels of the median values. Non-overlapping notches indicate that the median values are significantly different from each other.

the southeast; Li et al., 2007) and at Xinglong (40.396°N , 117.578°E), which is located at the top of a mountain (970 m above sea level) ~ 100 km away from Beijing to the northwest (Zhu et al., 2014). Local pollutants and the products of their photochemical reactions, which are strongly absorbing, are the primary sources of aerosols in the PRD region. The other sites mentioned are more susceptible to coarse-mode mineral dust and local emissions. The relatively higher values of SSA in October and in February are associated with a stronger swelling effect due to the greater occurrence of a humid atmosphere (Fig. 4).

The AE is an indicator of particle size. High values of AE mean that fine particles dominate, while low values mean that coarse particles dominate. The frequency distribution of AE (440–870 nm) in the PRD region is shown in Fig. 5a. The histograms of AE (440–870 nm) follow a Gaussian distribution, with a central value equal to ~ 1.3 . Other studies have shown that if $\text{AE} (440\text{--}870 \text{ nm}) < 0.75$, coarse-mode dust particles dominate, and if $\text{AE} (470\text{--}870 \text{ nm}) > 1.0$, mainly fine-mode anthropogenic particles are present. Values of AE (470–870 nm) between 0.75 and 1.0 suggest complicated aerosol modes (Eck et al., 2005; Yang et al., 2011; Wang et al., 2014). The frequency of occurrence of AE (440–870 nm) < 0.75 ranged from 0 in November and February to 1.83% in October. The proportion of AE (440–870 nm) between 0.75 and 1.2 varied from 6.54% in February to 17.43% in December. The majority of aerosols had an AE (440–870 nm) > 1.2, ranging from 80.97% in December to 93.46% in February. On the whole, during the dry season, aerosols in the PRD region are mainly fine-mode pollution particles ($\sim 84.66\%$) and floating dust aerosols ($\sim 14.44\%$). The presence of heavy dust is negligible ($\sim 0.90\%$).

Figure 5b shows notched box whisker plots of the monthly AE (440–870 nm). The mean value of AE (470–870 nm) was 1.33. AE (440–870 nm) values varied from 1.31 to 1.38 and were significantly higher in February and October ($p < 0.01$) and lower in December ($p < 0.01$), suggesting

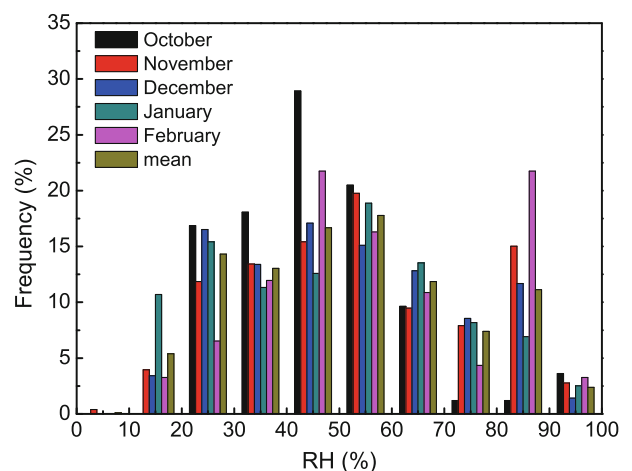


Fig. 4. Frequency distributions of RH. The frequency in each month was calculated using 10 RH bins ranging from 5% to 95%.

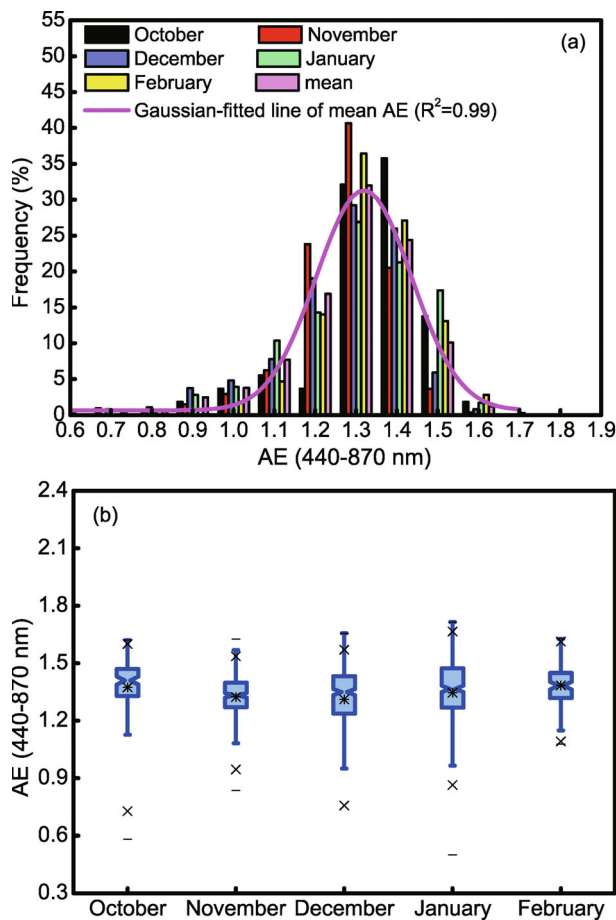


Fig. 5. (a) Frequency distributions of AE (440–870 nm) and (b) monthly variations in AE (440–870 nm) in the PRD region. The notches in the notched box and whisker plots represent the 95% confidence levels of the median values. Non-overlapping notches indicate that the median values are significantly different from each other.

a greater contribution of fine particles to extinction over the PRD region. The PRD region typically experiences high-humidity weather in February, when the background of cold air suddenly becomes warm air during the transition between winter and spring (Zhang et al., 2014). Frequent air mass stagnation episodes in February limit the diffusion of air, which results in higher AE (440–870 nm) due to anthropogenic aerosol pollution.

3.2. Aerosol characterization inferred from the AE (440–870 nm), ω , and volume size distributions

The wavelength dependence of ω provides more information about the physicochemical properties of aerosol types and the AE provides information about particle size (Logan et al., 2013). Therefore, these two parameters were combined to classify aerosol types in the PRD region.

As done by Logan et al. (2013) when examining data from sites in China and Thailand, $\omega = 0.07$ was chosen as the demarcation line between strongly and weakly absorbing aerosols, and $AE = 0.75$ was chosen as the demarcation line between fine-mode and coarse-mode particles. These thresh-

old values were deemed reasonable to use in this study because the PRD region is also primarily affected by pollution, biomass-burning aerosols, mineral dust, and complex mixtures of various particle types (Lai et al., 2007; Lee et al., 2007; Deng et al., 2008). Four regions were defined: Region I, where fine-mode, weakly absorbing particles dominate; Region II, where fine-mode, strongly absorbing particles dominate; Region III, where coarse-mode, strongly absorbing mineral dust particles dominate; and Region IV, where coarse-mode, weakly absorbing particles dominate, e.g., desert aerosols.

Figure 6 shows the mean classification results for the months of October to February of the years 2006–12. About 9.5% of all data points fell in Region I, i.e., the region representing fine-mode, weakly absorbing particles. Because few dust events take place in the PRD region, the number of data points in the coarse-mode regions (III and IV) was negligible. Up to 90% of all particles fell in region II, mainly in January (Fig. 6d). The majority of region II data points were centered on ω values between 0.07 and 0.17, and AE values between 1.2 and 1.5.

Overall, fine-mode, strongly absorbing aerosol particles were dominant in the study area. Given the location of Panyu, pollutants at the site are likely a combination of carbon aerosols [e.g., organic and black carbon (BC)] or mixtures of sulfate, nitrite, and carbon aerosols generated by vehicles and stoves (Andreae et al., 2008; Zheng et al., 2011; Wang et al., 2012). Compared to region II, aerosols in region I had a higher AOD (0.65) and larger particle size ($AE = 1.30$).

The average volume size distributions for different months are shown in Fig. 7. The column-integrated aerosol volume size distribution is bimodal, with a dominating fine mode (radius $< 1.16 \mu\text{m}$) and a coarse mode (radius $> 1.16 \mu\text{m}$). The peak in the fine mode was the same for all months (radius = $0.12 \mu\text{m}$). Peak volumes of the fine mode were higher in February and in October, which had almost equal values (0.11 and $0.10 \mu\text{m}^3 \mu\text{m}^{-2}$, respectively). Peak volumes were lower in the other months and ranged from 0.07 – $0.08 \mu\text{m}^3 \mu\text{m}^{-2}$. The coarse mode showed maxima in radii equal to 5.29 , 5.29 , 11.31 , 11.31 and $3.62 \mu\text{m}$ in October, November, December, January and February, with peak volumes of 0.033 , 0.031 , 0.038 , 0.037 and $0.028 \mu\text{m}^3 \mu\text{m}^{-2}$, respectively. Because dust events in the PRD region are scarce, the monthly coarse modes were similar, with a mean peak volume 0.43 times that of the peak volume in the fine mode. The lower tail of the coarse mode in February is likely the result of fine-mode contamination.

3.3. Diurnal radiative forcing and efficiency

In the PRD region, high aerosol loading prevails all year round, with an average AOD equal to 0.54. As a result, aerosols are expected to seriously impact irradiances reaching the earth's surface, which can significantly influence atmospheric stability and regional climate.

Previous studies have revealed that ADRF varies significantly in different regions and at different time scales (Xia et al., 2007a, 2016; Li et al., 2010). Other studies have reported

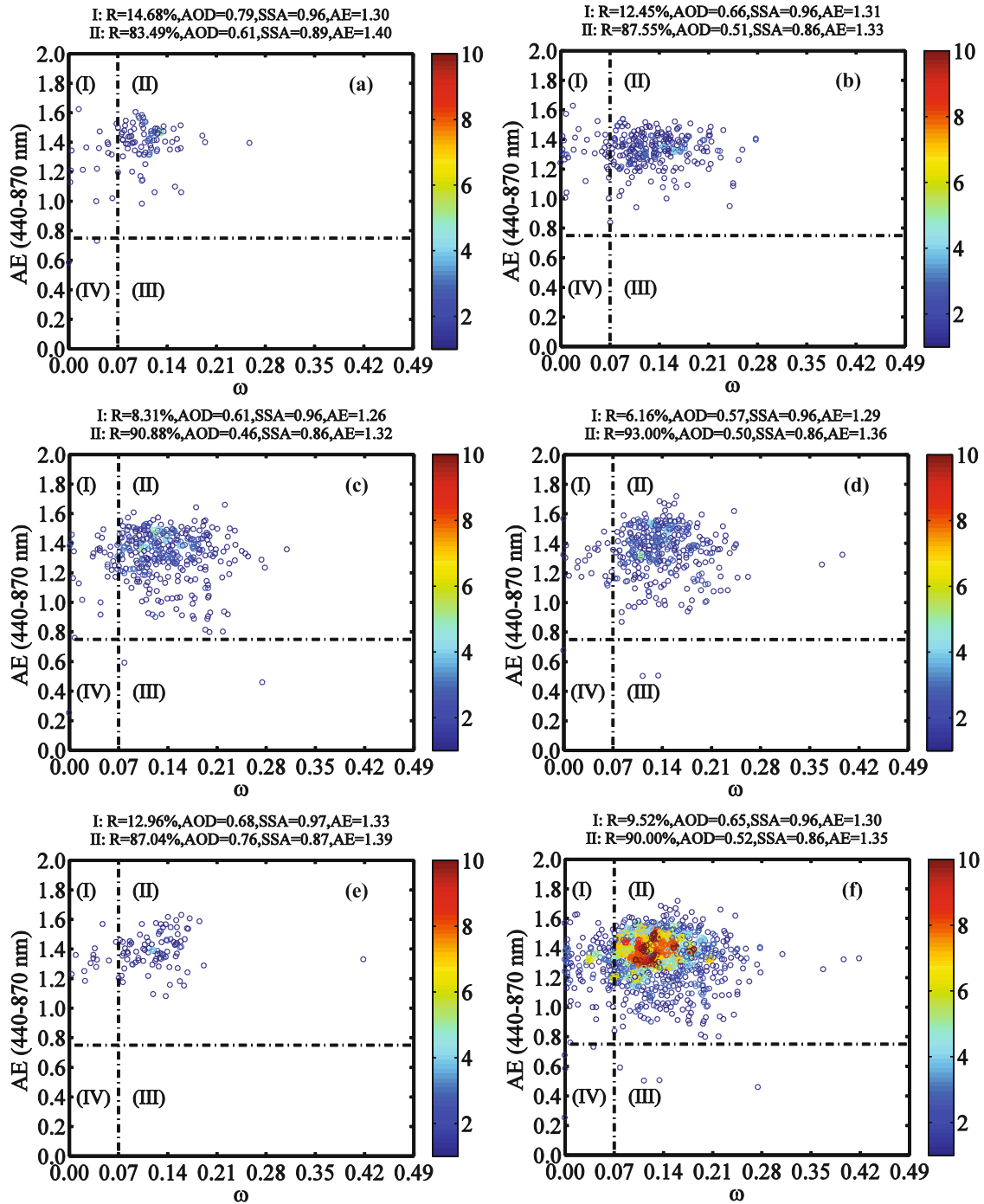


Fig. 6. Classification of the mean physicochemical properties of aerosols into four regions using AE (440–870 nm) and ω at 440 nm. The color scale represents the relative density of points. Panels (a–f) correspond to October, November, December, January, February, and all data, respectively, in the years 2006–12. R is the proportion of particle amount.

only instantaneous values of aerosol radiative forcing (e.g., Che et al., 2009b, 2014), which should not be compared with daily and annual averages. Annually averaged global values of F_{SFC} , F_{TOA} and F_{ATM} from satellite–model integrated approaches over land are -11.9 , -4.9 and 7.0 W m^{-2} , respectively, and from model simulations are -7.6 , -3.0 and 4.6 W m^{-2} , respectively (Yu et al., 2006). The monthly mean diurnal ADRF in the PRD region is shown in Fig. 8. The

largest monthly values were in February, when F_{SFC} and F_{ATM} reached -37.5 and 30.0 W m^{-2} , respectively. This happened because AOD values were high and SSA values were low in February. The average F_{SFC} , F_{ATM} and F_{TOA} was -33.4 ± 7.0 , 26.1 ± 5.6 and $-7.3 \pm 2.7 \text{ W m}^{-2}$, respectively. The large negative F_{SFC} and positive F_{ATM} suggests that more solar radiation is absorbed within the atmosphere, consequently warming the atmosphere, reducing eddy heat

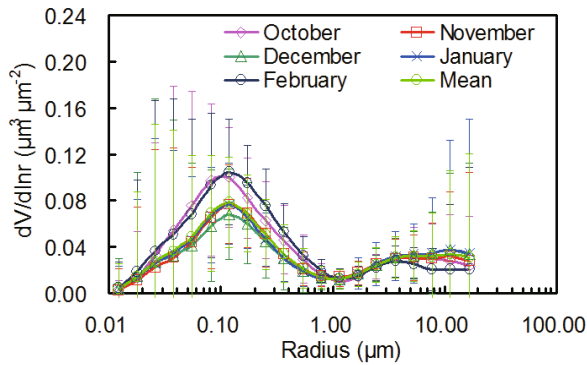


Fig. 7. Average volume size distributions of aerosols as a function of particle radius over the PRD region for different months. Error bars represent standard deviations.

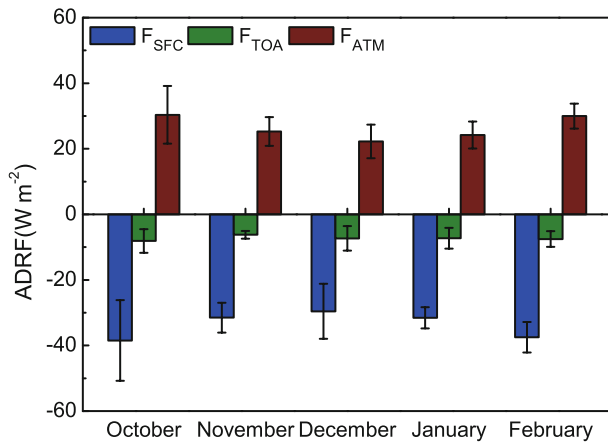


Fig. 8. Monthly mean diurnal ADRF at the surface (F_{SFC}), at the top of the atmosphere (F_{TOA}), and within the atmosphere (F_{ATM}). Error bars represent standard deviations.

convergence, and inducing a reduction in surface temperature, which ultimately affects regional climate (Liu et al., 2008; Ge et al., 2010). Figure 9 shows the diurnal ADRF at the surface, within the atmosphere, and at the TOA, as a function of AOD. The ADRF was almost linearly correlated with AOD. The standard deviations at the surface (3.5 W m^{-2}), at the TOA (1.96 W m^{-2}) and in the atmosphere (3.81 W m^{-2}) were much lower than the values reported by Li et al. (2010) (14.45 , 5.45 and 16.08 W m^{-2} , respectively). This is because the study region here is much smaller and there is little variation in aerosol composition, which is also suggested by the near constant magnitude of the SSA (Fig. 3b).

Figure 10 shows the interannual trends in diurnal ADRF during the dry season in the PRD region. The relative standard deviations of F_{SFC} , F_{TOA} and F_{ATM} were $\sim 20.96\%$, 36.99% and 21.46% , respectively. These values were less than those reported over China in general [56.96% to 533.33% (Li et al., 2010)] and in the Yangtze Delta region [26.15% to 58.54% (Liu et al., 2012)]. The lower values of the relative standard deviation are mostly due to relatively

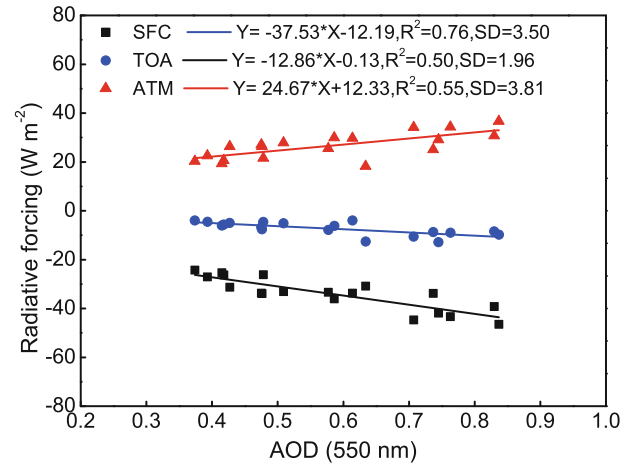


Fig. 9. Diurnal ADRF at the surface (SFC, black), at the top of the atmosphere (TOA, blue), and within the atmosphere (ATM, red) as a function of AOD at 550 nm over the PRD region. Best-fit lines through the points are shown and linear regression functions and statistics (coefficient of determination, R^2 , and standard deviation, SD) are given.

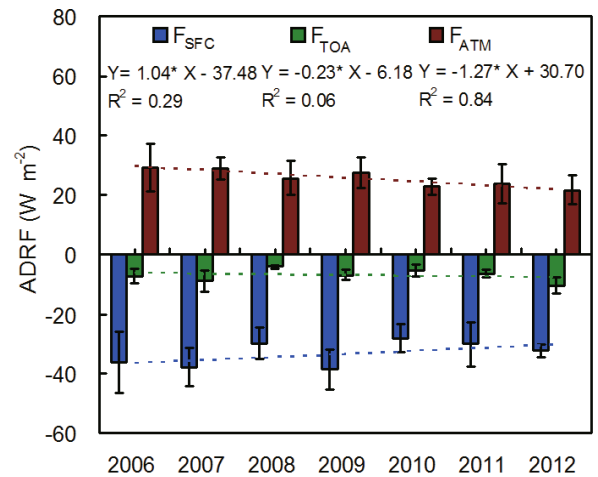


Fig. 10. Interannual trends in diurnal ADRF during the dry season (October to February) in the PRD region. Dashed red, green, and blue lines represent linear-fit lines for ADRF within the atmosphere (ATM), at the top of the atmosphere (TOA), and at the surface (SFC), respectively. Vertical bars represent one standard deviation computed from the monthly mean forcing.

less variation in aerosol composition and partly due to month-to-month changes in radiative forcing. The magnitudes of F_{SFC} varied from -36.2 W m^{-2} in 2006 to -32.3 W m^{-2} in 2012, and the magnitudes of F_{TOA} varied from -7.2 W m^{-2} in 2006 to -10.6 W m^{-2} in 2012. Both of these trends did not pass the 99% confidence level of the t -test ($p < 0.01$; $r_{SFC} = 0.53$, $r_{TOA} = 0.24$; $n = 6$). By contrast, F_{ATM} varied from -29.1 W m^{-2} in 2006 to -21.7 W m^{-2} in 2012, and this trend was statistically significant ($p < 0.01$; $r_{ATM} = 0.92$; $n = 6$). Moreover, the SSA increased from 0.87 in 2006 to 0.91 in 2012, and the fine-mode aerosol concentration such

as $PM_{2.5}$ decreased from $69.5 \mu g m^{-3}$ in 2006 to $45.0 \mu g m^{-3}$ in 2012. These results suggest a trend of less-absorbing particles being released into the atmosphere during the study period. This phenomenon is most likely due to the pollutant-controlling measures executed by the local government. In recent years, the local government has implemented a series of control measures with respect to emissions from coal burning, motor vehicle exhaust, and industrial sectors, which has resulted in an apparent decrease in the number of hazy days (<http://www.gzepb.gov.cn/>, in Chinese) and the amount of $PM_{2.5}$ (Wang et al., 2016). Owing to these measures, concentrations of carbonaceous aerosols, such as organic carbon and elemental carbon, have shown a decreasing trend (Fu et al., 2014; Wang et al., 2016). The weaker radiative forcing in 2010 may be attributable to the stricter emission reduction measures in place during the 2010 Asia Games held in Guanzhou, resulting in AOD reducing to 0.43, and $PM_{2.5}$ and elemental carbon concentrations decreasing by 29% and 49%, respectively (Hu et al., 2013).

Table 1 summarizes the ADRF over the PRD and other regions. The presence of anthropogenic aerosols over the PRD region can considerably decrease surface and TOA forcings and enhance atmospheric forcing. The magnitudes of the mean F_{SFC} and F_{ATM} in this study region are about two times greater than that reported over the whole of China, but are similar to those reported in the Yangtze Delta region and in northern China where anthropogenic and dust aerosols dominate. Relatively high RH over the PRD region can partly explain the larger aerosol cooling effect at the surface compared to that over the whole China region because RH strongly influences the ADRF estimated within the surface boundary layer (Cheng et al., 2008). Enhanced warming within the atmosphere is not surprising because an abundance of absorbing aerosol particles like BC is predominant in the PRD region (Wu et al., 2009). The F_{TOA} can change from negative to large positive forcing depending on the cloud fraction, surface albedo, and the vertical distributions of aerosols and clouds. However, regional TOA direct forcing is highly uncertain, particularly in regions containing atmospheric pollution like India (Ramanathan et al., 2001) and China (Li et al., 2010). The magnitude of F_{TOA} was higher than values reported for the whole of China (Li et al., 2010), but similar to that in the Yangtze Delta region, which implies that abundant anthropogenic aerosols further cool the atmosphere–surface system over the polluted PRD region. However, the huge amount of solar radiation trapped inside the atmosphere is a significant source of heating for the atmosphere, particularly within the lower atmosphere, which can substantially alter the atmospheric stability and influence the dynamic system (Li et al., 2010).

The aerosol radiative FE is commonly used to quantify the radiative forcing potential of a given type of composite aerosol (Pathak et al., 2010). The diurnal mean FEs over the PRD and other regions are summarized in Table 2. The average FEs in this study were $-60.0 \pm 7.8 W m^{-2}$ per AOD at the surface, $-12.8 \pm 3.1 W m^{-2}$ per AOD at the TOA, and $47.3 \pm 8.3 W m^{-2}$ per AOD within the atmosphere. The

Table 1. Summary of aerosol direct radiative forcing over the PRD and other regions. Units: $W m^{-2}$. The AOD and SSA in this study were calculated as monthly mean values.

Aerosol Type	F_{SFC}	F_{TOA}	F_{ATM}	AOD	SSA	Location	Date	Source
ANT	-33.4 ± 7.0	-7.3 ± 2.7	26.1 ± 5.6	0.57 ± 0.16 (550 nm)	0.88 ± 0.02 (440 nm)	PRD	October–February, 2006–2012	This study
ANT, dust	-15.7 ± 8.9	0.3 ± 1.6	16.0 ± 9.2	0.69 (550 nm)	0.89 (550 nm)	China	2005	Li et al. (2010)
ANT	-61.0 ± 9.0	-14 ± 8	47.0 ± 9.0	0.67 ± 0.19 (500 nm)	0.93 ± 0.03 (500 nm)	Shandong Peninsula	2004–2011	Xin et al. (2014)
ANT, dust	-34.8 ± 9.1	-8.2 ± 4.8	26.7 ± 9.4	0.74 ± 0.45 (500 nm)	0.89 ± 0.04 (440 nm)	Yangtze Delta region	June 2008 to May 2009	Liu et al. (2012)
ANT, dust	-33.5	-11.3	22.2	n/a	n/a	Northern China	March 2001 to October 2005	Xia et al. (2007b)
Dust	-70.0	0.7	70.7	0.57 (500 nm)	0.87 (500 nm)	Loess Plateau, China	Dust event in spring 2009	Liu et al. (2011)
ANT	-73.0 ± 12.0	-22.0 ± 6.0	51.0 ± 13.0	0.48 ± 0.18 (500 nm)	0.91 ± 0.01 (500 nm)	Karachi, Pakistan	August 2006 to July 2007	Alam et al. (2011)

Note: ANT, anthropogenic; n/a, not available

Table 2. Radiative forcing efficiency over the PRD and other regions. Units: $W m^{-2} \tau^{-1}$.

Aerosol Type	FE _{SFC}	FE _{TOA}	FE _{ATM}	AOD	SSA	Location	Date	Source
ANT	-60.0±7.8	-12.8±3.1	47.3±8.3	0.57±0.16 (550 nm)	0.88±0.02 (440 nm)	PRD	October–February, 2006–2012	This study
ANT, dust	-35.1	-0.5	34.5	0.69 (500 nm)	0.89 (500 nm)	China	2005	Li et al. (2010)
ANT, dust	-61.2±3.5	-6.6±1.4	54.6±4.1	n/a	n/a	Beijing, China	2005	Li et al. (2010)
ANT, dust	-65.4±4.7	-2.9±1.9	62.5±3.7	n/a	n/a	Xianghe, China	2005	Li et al. (2010)
ANT, dust	-32.9±3.1	-5.5±0.6	27.4±3.1	n/a	n/a	Taihu, China	2005	Li et al. (2010)
BB	-37.6±1.6	0.43±1.5	38.0±0.6	n/a	n/a	Dinghu Mt.	2005	Li et al. (2010)
Dust	-106.0 to -91.0	-26.0 to -12.0	65.0 to 94.0	n/a	0.71–0.76 (500 nm)	Korea and Japan	April 2001	Kim et al. (2005)
Dust, ANT, BB	-76.0 to -63.0	-16.0 to -9.0	39.0 to 67.0	n/a	0.88–0.90 (500 nm)	East Asia	May 1997 to April 2001	Kim et al. (2005)
ANT	-91.0	-20.9	70.1	0.67±0.19 (500 nm)	0.93±0.03 (500 nm)	Shandong Peninsula	2004–2011	Xin et al. (2014)
Dust	-58.9	7.3	n/a	0.28 (500 nm)	0.88 (500 nm)	Yinchuan, Northwest China	October 2003 to August 2004	Liu et al. (2008)
OC+BC	-89.4	-15.0	n/a	0.015±0.038 (550 nm)	0.21 (550 nm)	South Asia	March 2001	Wang et al. (2007)

Note: ANT, anthropogenic; OC, organic carbon; BB, black carbon; BC, biomass burning; KCO, Kaashidhoo Climate Observatory; n/a, not available

magnitudes of these values are significantly higher than those reported in Taihu and over China as a whole. This is mainly due to the influence of strongly absorbing particles (e.g., carbonaceous aerosols), which reduce the net radiation at the surface and outgoing radiation at the TOA. As a result, atmospheric absorption increases. The magnitudes of the FEs are similar to those reported in Beijing, Xianghe, Yinchuan, East Asia, and at the Kaashidhoo Climate Observatory in the Maldives, but less than the values reported in South Asia and the Shandong Peninsula in China, where anthropogenic aerosols, BC, and organic carbon aerosols dominate (Wang et al., 2007; Xin et al., 2014).

4. Conclusions

Aerosol optical and radiative properties, including frequency, temporal variability, classification, and the interannual trends of radiative forcing, were derived and analyzed using seven years (2006–12) of ground-based measurements made at Panyu, the first observation site of CARSNET in the PRD region. The major conclusions can be summarized as follows:

(1) In the dry season (October to February), the average values of the AE (440–870 nm), SSA and AOD of aerosols in the PRD region were 1.33, 0.87 and 0.54, respectively. The occurrence of high AOD values indicates that heavy aerosol loading prevails in the dry season. Low AOD values most likely arise from the wet scavenging of aerosols after precipitation.

(2) Aerosols in the PRD region during the study period consisted primarily of fine-mode, strongly absorbing particles. Up to 90% of aerosols were dominated by fine-mode, strongly absorbing particles, with mean AE = 1.35, $\omega = 0.14$, and AOD = 0.52. The proportion of fine-mode, weakly absorbing particles was about 9.52%, with AE = 1.30, $\omega = 0.04$, and AOD = 0.65. Due to the minimal presence of dust in the PRD region, the aerosol coarse mode was negligible. The aerosol volume size distribution for each month was bimodal, with the fine mode dominating. The fine mode showed a peak at a radius of 0.12 μm in all months. Peak volumes were higher in February (0.11 $\mu m^3 \mu m^{-2}$) and in October (0.10 $\mu m^3 \mu m^{-2}$) than in the other months. The mean peak volume of the coarse mode was 0.43 times that of the peak volume in the fine mode.

(3) Heavy aerosol loading in the PRD region during the study period resulted in significant warming of the atmosphere and cooling at the surface. The average shortwave direct radiative forcing at the surface, inside the atmosphere, and at the TOA was -33.4 ± 7.0 , 26.1 ± 5.6 and $-7.3 \pm 2.7 W m^{-2}$, respectively. The magnitudes of mean F_{SFC} and F_{ATM} were about two times greater than that reported over the whole of China, but similar to those reported in the Yangtze Delta region and in northern China. The corresponding average aerosol direct shortwave radiative forcing efficiencies were -60.0 ± 7.8 , 47.3 ± 8.3 and $-12.8 \pm 3.1 W m^{-2}$ per AOD, respectively, mainly due to the influence of strongly absorb-

ing particles (e.g., carbonaceous aerosols), which reduce the net radiation at the surface and outgoing radiation at the TOA.

(4) The aerosol direct radiative forcing within the atmosphere was reduced significantly during the study period ($p < 0.01$). Moreover, the SSA increased from 0.87 in 2006 to 0.91 in 2012, and the fine-mode aerosol concentration such as $PM_{2.5}$ decreased from $69.5 \mu\text{g m}^{-3}$ in 2006 to $45.0 \mu\text{g m}^{-3}$ in 2012. These results suggest a decreasing trend of absorbing particles being released into the atmosphere.

(5) Given that aerosol radiative properties and forcing have not been as thoroughly examined in the PRD region compared to the rest of China, these results can help constrain uncertainties in estimating regional anthropogenic aerosol radiative forcing. In future work, more attention will be paid to the source and distribution of aerosols using satellite-based aerosol measurements along with a priori knowledge of the optical properties of likely aerosol types. The results of this study can be used to improve inversion algorithms for satellite aerosol retrievals over the PRD region, such as those from MODIS and the Multi-angle Imaging Spectroradiometer. In addition, the strong aerosol radiative forcing mainly caused by absorbing particles reported here can provide better constraints for assessing aerosol climate effects in climate models.

Acknowledgements. This research was funded by the National Natural Science Foundation of China (Grant Nos. 41475105, 41475138, 41405133 and 41605105), the National Key Project of MOST (Grant No. 2016YFC0202003, 2016YFC0203305, 2016YFC0201901), the Guangdong Province Science and Technology Plan (Grant No. 2015A020215020), the Science and Technology Innovative Research Team Plan of Guangdong Meteorological Bureau (Grant No. 201506), and the Science and Technology Research Project of Guangdong Meteorological Bureau (Grant No. 2015B06). The availability of the data used for this study is fully described in section 2 of the paper. The MODIS data were downloaded from the NASA Goddard Space Flight Center. We also thank the developers of the SKYRAD.pack software package and the SB-DART model, and the staff at the Hong Kong Polytechnic University AERONET site. The constructive suggestions from the anonymous reviewers were greatly appreciated.

REFERENCES

- Ackerman, A. S., O. B. Toon, D. E. Stevens, A. J. Heymsfield, V. Ramanathan, and E. J. Welton, 2000: Reduction of tropical cloudiness by soot. *Science*, **288**, 1042–1047, <https://doi.org/10.1126/science.288.5468.1042>.
- Anderson, T. L., S. J. Masonis, D. S. Covert, N. C. Ahlquist, S. G. Howell, A. D. Clarke, and C. S. McNaughton, 2003: Variability of aerosol optical properties derived from in situ aircraft measurements during ACE-Asia. *J. Geophys. Res.*, **108**(D23), 8647, <https://doi.org/10.1029/2002JD003247>.
- Andreae, M. O., O. Schmid, H. Yang, D. Chand, J. Z. Yu, L.-M. Zeng, and Y.-H. Zhang, 2008: Optical properties and chemical composition of the atmospheric aerosol in urban Guangzhou, China. *Atmos. Environ.*, **42**, 6335–6350, <https://doi.org/10.1016/j.atmosenv.2008.01.030>.
- Ångström, A., 1964: The parameters of atmospheric turbidity. *Tellus*, **16**(1), 64–75.
- Behnert, I., V. Matthias, and R. Doerffler, 2007: Aerosol climatology from ground-based measurements for the southern North Sea. *Atmos. Res.*, **84**, 201–220, <https://doi.org/10.1016/j.atmosres.2006.05.006>.
- Bokoye, A. I., A. Royer, N. T. O'Neill, P. Cliche, G. Fedosejevs, P. M. Teillet, and L. J. B. McArthur, 2001: Characterization of atmospheric aerosols across Canada from a ground-based sunphotometer network: AEROCAN. *Atmos.-Ocean*, **39**, 429–456, <https://doi.org/10.1080/07055900.2001.9649687>.
- Cao, J. J., S. C. Lee, K. F. Ho, X. Y. Zhang, S. C. Zou, K. Fung, J. C. Chow, and J. G. Watson, 2003: Characteristics of carbonaceous aerosol in Pearl River Delta Region, China during 2001 winter period. *Atmos. Environ.*, **37**, 1451–1460, [https://doi.org/10.1016/S1352-2310\(02\)01002-6](https://doi.org/10.1016/S1352-2310(02)01002-6).
- Cao, J. J., S. C. Lee, K. F. Ho, S. C. Zou, K. Fung, Y. Li, J. G. Watson, and J. C. Chow, 2004: Spatial and seasonal variations of atmospheric organic carbon and elemental carbon in Pearl River Delta region, China. *Atmos. Environ.*, **38**, 4447–4456, <https://doi.org/10.1016/j.atmosenv.2004.05.016>.
- Chameides, W. L., and Coauthors H, 1999: Case study of the effects of atmospheric aerosols and regional haze on agriculture: An opportunity to enhance crop yields in China through emission controls? *Proc. Natl. Acad. Sci. U. S. A.*, **96**, 13 626–13 633, <https://doi.org/10.1073/pnas.96.24.13626>.
- Che, H., G. Shi, A. Uchiyama, A. Yamazaki, H. Chen, P. Goloub, and X. Zhang, 2008: Intercomparison between aerosol optical properties by a PREDE sky radiometer and CIMEL sunphotometer over Beijing, China. *Atmos. Chem. Phys.*, **8**, 3199–3214, <https://doi.org/10.5194/acp-8-3199-2008>.
- Che, H., and Coauthors, 2014: Column aerosol optical properties and aerosol radiative forcing during a serious haze-fog month over North China Plain in 2013 based on ground-based sunphotometer measurements. *Atmos. Chem. Phys.*, **14**, 2125–2138, <https://doi.org/10.5194/acp-14-2125-2014>.
- Che, H., and Coauthors, 2015: Ground-based aerosol climatology of China: Aerosol optical depths from the China Aerosol Remote Sensing Network (CARSNET) 2002–2013. *Atmos. Chem. Phys.*, **15**, 7619–7652, <https://doi.org/10.5194/acp-15-7619-2015>.
- Che, H. Z., and Coauthors, 2009a: Instrument calibration and aerosol optical depth validation of the China Aerosol Remote Sensing Network. *J. Geophys. Res.*, **114**, D03206, <https://doi.org/10.1029/2008JD011030>.
- Che, H. Z., X. Y. Zhang, S. Alfraro, B. Chatenet, L. Gomes, and J. Q. Zhao, 2009b: Aerosol optical properties and its radiative forcing over Yulin, China in 2001 and 2002. *Adv. Atmos. Sci.*, **26**(3), 564–576, <https://doi.org/10.1007/s00376-009-0564-4>.
- Cheng, Y. F., and Coauthors, 2008: Aerosol optical properties and related chemical apportionment at Xinken in Pearl River Delta of China. *Atmos. Environ.*, **42**, 6351–6372, <https://doi.org/10.1016/j.atmosenv.2008.02.034>.
- Clarke, A., and V. Kapustin, 2010: Hemispheric aerosol vertical profiles: Anthropogenic impacts on optical depth and cloud nuclei. *Science*, **329**, 1488–1492, <https://doi.org/10.1126/science.1188838>.
- Corrigan, C. E., V. Ramanathan, and J. J. Schauer, 2006: Impact of monsoon transitions on the physical and optical properties of aerosols. *J. Geophys. Res.*, **111**, D18208, <https://doi.org/10.1029/2005JD006370>.
- Deng, X. J., and Coauthors, 2008: Effects of Southeast Asia

- biomass burning on aerosols and ozone concentrations over the Pearl River Delta (PRD) region. *Atmos. Environ.*, **42**(36), 8439–8501, <https://doi.org/10.1016/j.atmosenv.2008.08.013>.
- Deng, X. J., and Coauthors, 2011: Effect of atmospheric aerosol on surface ozone variation over the Pearl River Delta region. *Science China Earth Sciences*, **54**, 744–752, <https://doi.org/10.1007/s11430-011-4172-7>.
- Eck, T. F., B. N. Holben, J. S. Reid, O. Dubovik, A. Smirnov, N. T. O'Neill, I. Slutsker, and S. Kinne, 1999: Wavelength dependence of the optical depth of biomass burning, urban, and desert dust aerosols. *J. Geophys. Res.*, **104**, 31 333–31 349, <https://doi.org/10.1029/1999JD900923>.
- Eck, T. F., and Coauthors, 2005: Columnar aerosol optical properties at AERONET sites in central eastern Asia and aerosol transport to the tropical mid-Pacific. *J. Geophys. Res.*, **110**, D06202, <https://doi.org/10.1029/2004JD005274>.
- Fu, X. X., and Coauthors, 2014: Trends of ambient fine particles and major chemical components in the Pearl River Delta region: Observation at a regional background site in fall and winter. *Science of the Total Environment*, **497–498**, 274–281, <https://doi.org/10.1016/j.scitotenv.2014.08.008>.
- Ge, J. M., J. Su, T. P. Ackerman, Q. Fu, J. P. Huang, and J. S. Shi, 2010: Dust aerosol optical properties retrieval and radiative forcing over northwestern China during the 2008 China-U.S. joint field experiment. *J. Geophys. Res.*, **115**, D00K12, <https://doi.org/10.1029/2009JD013263>.
- Gobbi, G. P., Y. J. Kaufman, I. Koren, and T. F. Eck, 2007: Classification of aerosol properties derived from AERONET direct sun data. *Atmospheric Chemistry and Physics*, **7**, 453–458, <https://doi.org/10.5194/acp-7-453-2007>.
- Guo, J. P., and Coauthors, 2016: Delaying precipitation and lightning by air pollution over the Pearl River Delta. Part I: Observational analyses. *J. Geophys. Res.*, **121**, 6472–6488, <https://doi.org/10.1002/2015JD023257>.
- Halthore, R. N., and Coauthors, 2005: Intercomparison of short-wave radiative transfer codes and measurements. *J. Geophys. Res.*, **110**, D11206, <https://doi.org/10.1029/2004JD005293>.
- Holben, B. N., and Coauthors, 1998: AERONET-A federated instrument network and data archive for aerosol characterization. *Remote Sensing of Environment*, **66**, 1–16, [https://doi.org/10.1016/S0034-4257\(98\)00031-5](https://doi.org/10.1016/S0034-4257(98)00031-5).
- Hu, W., M. Hu, Q. Tang, S. Guo, and C. Q. Yan, 2013: Characterization of particulate pollution during Asian Games in Pearl River Delta (PRD) region. *Acta Scientiae Circumstantiae*, **33**(7), 1815–1823. (in Chinese)
- IPCC, 2013: Climate Change 2013: The Physical Science Basis. *Contribution of Working Group I to the Fifth Assessment Report of the Intergovernmental Panel on Climate Change*, T. F. Stocker et al., Eds., Cambridge University Press, Cambridge, United Kingdom and New York, NY, USA, 1535 pp, <https://doi.org/10.1017/CBO9781107415324>.
- Khatri, P., T. Takamura, A. Shimizu, and N. Sugimoto, 2014: Observation of low single scattering albedo of aerosols in the downwind of the East Asian desert and urban areas during the inflow of dust aerosols. *J. Geophys. Res.*, **119**, 787–802, <https://doi.org/10.1002/2013JD019961>.
- Kim, D.-H., B.-J. Sohn, T. Nakajima, and T. Takamura, 2005: Aerosol radiative forcing over East Asia determined from ground-based solar radiation measurements. *J. Geophys. Res.*, **110**, D10S22, <https://doi.org/10.1029/2004JD004678>.
- Koren, I., Y. J. Kaufman, L. A. Remer, and J. V. Martins, 2004: Measurement of the effect of Amazon smoke on inhibition of cloud formation. *Science*, **303**(5662), 1342–1345, <https://doi.org/10.1126/science.1089424>.
- Kosmopoulos, P. G., D. G. Kaskaoutis, P. T. Nastos, and H. D. Kambezidis, 2008: Seasonal variation of columnar aerosol optical properties over Athens, Greece, based on MODIS data. *Remote Sensing of Environment*, **112**, 2354–2366, <https://doi.org/10.1016/j.rse.2007.11.006>.
- Lai, S.-C., S.-C. Zou, J.-J. Cao, S.-C. Lee, and K.-F. Ho, 2007: Characterizing ionic species in PM_{2.5} and PM₁₀ in four Pearl River Delta cities, South China. *Journal of Environmental Sciences*, **19**, 939–947, [https://doi.org/10.1016/S1001-0742\(07\)60155-7](https://doi.org/10.1016/S1001-0742(07)60155-7).
- Lee, C. S. L., X.-D. Li, G. Zhang, J. Li, A.-J. Ding, and T. Wang, 2007: Heavy metals and Pb isotopic composition of aerosols in urban and suburban areas of Hong Kong and Guangzhou, South China—Evidence of the long-range transport of air contaminants. *Atmos. Environ.*, **41**(2), 432–447, <https://doi.org/10.1016/j.atmosenv.2006.07.035>.
- Li, Z. Q., and Coauthors, 2007: Aerosol optical properties and their radiative effects in northern China. *J. Geophys. Res.*, **112**, D22S01, <https://doi.org/10.1029/2006JD007382>.
- Li, Z. Q., K.-H. Lee, Y. S. Wang, J. Y. Xin, and W.-M. Hao, 2010: First observation-based estimates of cloud-free aerosol radiative forcing across China. *J. Geophys. Res.*, **115**, D00K18, <https://doi.org/10.1029/2009JD013306>.
- Li, Z. Q., and Coauthors, 2016: Aerosol and monsoon climate interactions over Asia. *Rev. Geophys.*, **54**(4), 866–929, <https://doi.org/10.1002/2015RG000500>.
- Liang, S. L., 2001: Narrowband to broadband conversions of land surface albedo. I: Algorithms. *Remote Sensing of Environment*, **76**, 213–238, [https://doi.org/10.1016/S0034-4257\(00\)00205-4](https://doi.org/10.1016/S0034-4257(00)00205-4).
- Liu, J., X. Xia, P. Wang, Z. Li, Y. Zheng, M. Cribb, and H. Chen, 2007: Significant aerosol direct radiative effects during a pollution episode in northern China. *Geophys. Res. Lett.*, **34**, L23808, <https://doi.org/10.1029/2007GL030953>.
- Liu, J. J., Y. F. Zheng, Z. Q. Li, and R. J. Wu, 2008: Ground-based remote sensing of aerosol optical properties in one city in northwest China. *Atmos. Res.*, **89**, 194–205, <https://doi.org/10.1016/j.atmosres.2008.01.010>.
- Liu, J. J., Y. F. Zheng, Z. Q. Li, C. Flynn, and M. Cribb, 2012: Seasonal variations of aerosol optical properties, vertical distribution and associated radiative effects in the Yangtze Delta region of China. *J. Geophys. Res.*, **117**, D00K38, <https://doi.org/10.1029/2011JD016490>.
- Liu, Y., and Coauthors, 2011: Aerosol optical properties and radiative effect determined from sky-radiometer over Loess Plateau of Northwest China. *Atmos. Chem. Phys.*, **11**, 11 455–11 463, <https://doi.org/10.5194/acp-11-11455-2011>.
- Logan, T., B. Xi, X. Dong, Z. Li, and M. Cribb, 2013: Classification and investigation of Asian aerosol absorptive properties. *Atmos. Chem. Phys.*, **13**, 2253–2265, <https://doi.org/10.5194/acp-13-2253-2013>.
- McClatchey, R. A., R. W. Fenn, J. E. A. Selby, F. E. Volz, and J. S. Garing, 1972: *Optical Properties of the Atmosphere*. 3rd ed. Air Force Cambridge Research Laboratory, Bedford, MA, USA, 113 pp.
- Mitchell, R. M., and B. W. Forgan, 2003: Aerosol measurement in the Australian outback: Intercomparison of sun photometers. *J. Atmos. Oceanic Technol.*, **20**, 54–66, [https://doi.org/10.1175/1520-0426\(2003\)020<0054:AMITAO>2.0.CO;2](https://doi.org/10.1175/1520-0426(2003)020<0054:AMITAO>2.0.CO;2).
- Nakajima, T., G. Tonna, R. Z. Rao, P. Boi, Y. J. Kaufman, and

- B. Holben, 1996: Use of sky brightness measurements from ground for remote sensing of particulate polydispersions. *Appl. Opt.*, **35**(15), 2672–2686, <https://doi.org/10.1364/AO.35.002672>.
- Nakajima, T., and Coauthors, 2003: Significance of direct and indirect radiative forcings of aerosols in the East China Sea region. *J. Geophys. Res.*, **108**(D23), 8658, <https://doi.org/10.1029/2002JD003261>.
- Pathak, B., G. Kalita, K. Bhuyan, P. K. Bhuyan, and K. K. Moorthy, 2010: Aerosol temporal characteristics and its impact on shortwave radiative forcing at a location in the northeast of India. *J. Geophys. Res.*, **115**, D19204, <https://doi.org/10.1029/2009JD013462>.
- Qin, Y., and R. M. Mitchell, 2009: Characterisation of episodic aerosol types over the Australian continent. *Atmos. Chem. Phys.*, **9**(6), 1943–1956, <https://doi.org/10.5194/acp-9-1943-2009>.
- Ramanathan, V., and Coauthors, 2001: Indian Ocean experiment: An integrated analysis of the climate forcing and effects of the great Indo-Asian haze. *J. Geophys. Res.*, **106**, 28 371–28 398, <https://doi.org/10.1029/2001JD900133>.
- Ricchiazzi, P., S. R. Yang, C. Gautier, and D. Sowle, 1998: SB-DART: A research and teaching software tool for plane-parallel radiative transfer in the Earth's atmosphere. *Bull. Amer. Meteor. Soc.*, **79**, 2101–2114, [https://doi.org/10.1175/1520-0477\(1998\)079<2101:SARATS>2.0.CO;2](https://doi.org/10.1175/1520-0477(1998)079<2101:SARATS>2.0.CO;2).
- Rosenfeld, D., U. Lohmann, G. B. Raga, C. D. O'Dowd, M. Kulmala, S. Fuzzi, A. Reissell, and M. O. Andreae, 2008: Flood or drought: How do aerosols affect precipitation? *Science*, **321**, 1309–1313, <https://doi.org/10.1126/science.1160606>.
- Smirnov, A., B. N. Holben, T. F. Eck, O. Dubovik, and I. Slutsker, 2000: Cloud-screening and quality control algorithms for the AERONET database. *Remote Sensing of Environment*, **73**, 337–349, [https://doi.org/10.1016/S0034-4257\(00\)00109-7](https://doi.org/10.1016/S0034-4257(00)00109-7).
- Tao, R., and Coauthors, 2014: Development of an integrating sphere calibration method for Cimel sunphotometers in China aerosol remote sensing network. *Particuology*, **13**, 88–99, <https://doi.org/10.1016/j.partic.2013.04.009>.
- Valenzuela, A., F. J. Olmo, H. Lyamani, M. Antón, A. Quirantes, and L. Alados-Arboledas, 2012: Classification of aerosol radiative properties during African desert dust intrusions over southeastern Spain by sector origins and cluster analysis. *J. Geophys. Res.*, **117**, D06214, <https://doi.org/10.1029/2011JD016885>.
- Wang, M. X., 1999: *Atmospheric Chemistry*. China Meteorological Press, Beijing. (in Chinese)
- Wang, P., H. Z. Che, X. C. Zhang, Q. L. Song, Y. Q. Wang, Z. H. Zhang, X. Dai, and D. J. Yu, 2010: Aerosol optical properties of regional background atmosphere in Northeast China. *Atmos. Environ.*, **44**, 4404–4412, <https://doi.org/10.1016/j.atmosenv.2010.07.043>.
- Wang, S.-H., N.-H. Lin, M.-D. Chou, and J.-H. Woo, 2007: Estimate of radiative forcing of Asian biomass-burning aerosols during the period of TRACE-P. *J. Geophys. Res.*, **112**, D10222, <https://doi.org/10.1029/2006JD007564>.
- Wang, X. M., W. H. Chen, D. H. Chen, Z. Y. Wu, and Q. Fan, 2016: Long-term trends of fine particulate matter and chemical composition in the Pearl River Delta Economic Zone (PRDEZ), China. *Frontiers of Environmental Science & Engineering*, **10**(1), 53–62, <https://doi.org/10.1007/s11783-014-0728-z>.
- Wang, X. M., X. Ding, X. X. Fu, Q. F. He, S. Y. Wang, F. Bernard, X. Y. Zhao, and D. Wu, 2012: Aerosol scattering coefficients and major chemical compositions of fine particles observed at a rural site in the central Pearl River Delta, South China. *Journal of Environmental Sciences*, **24**(1), 72–77, [https://doi.org/10.1016/S1001-0742\(11\)60730-4](https://doi.org/10.1016/S1001-0742(11)60730-4).
- Wang, Z. Z., D. Liu, Z. E. Wang, Y. J. Wang, P. Khatri, J. Zhou, T. Takamura, and G. Y. Shi, 2014: Seasonal characteristics of aerosol optical properties at the SKYNET Hefei site (31.90°N, 117.17°E) from 2007 to 2013. *J. Geophys. Res.*, **119**, 6128–6139, <https://doi.org/10.1002/2014JD021500>.
- Wu, D., and Coauthors, 2009: Black carbon aerosols and their radiative properties in the Pearl River Delta region. *Science in China Series D: Earth Sciences*, **52**(8), 1152–1163, <https://doi.org/10.1007/s11430-009-0115-y>.
- Xia, X., H. Chen, P. Goloub, W. Zhang, B. Chatenet, and P. Wang, 2007b: A compilation of aerosol optical properties and calculation of direct radiative forcing over an urban region in northern China. *J. Geophys. Res.*, **112**, D12203, <https://doi.org/10.1029/2006JD008119>.
- Xia, X., Z. Li, P. Wang, H. Chen, and M. Cribb, 2007d: Estimation of aerosol effects on surface irradiance based on measurements and radiative transfer model simulations in northern China. *J. Geophys. Res.*, **112**, D22S10, <https://doi.org/10.1029/2006JD008337>.
- Xia, X., and Coauthors, 2016: Ground-based remote sensing of aerosol climatology in China: Aerosol optical properties, direct radiative effect and its parameterization. *Atmos. Environ.*, **124**, 243–251, <https://doi.org/10.1016/j.atmosenv.2015.05.071>.
- Xia, X. A., P. C. Wang, H. B. Chen, P. Gouloub, and W. X. Zhang, 2005: Ground-based remote sensing of aerosol optical properties over north China in spring. *Journal of Remote Sensing*, **9**(4), 429–437, <https://doi.org/10.3321/j.issn:1007-4619.2005.04.014>. (in Chinese with English abstract)
- Xia, X. G., Z. Q. Li, B. Holben, P. C. Wang, T. Eck, H. B. Chen, M. Cribb, and Y. X. Zhao, 2007a: Aerosol optical properties and radiative effects in the Yangtze Delta region of China. *J. Geophys. Res.*, **112**, D22S12, <https://doi.org/10.1029/2007JD008859>.
- Xia, X. G., H. B. Chen, Z. Q. Li, P. C. Wang, and J. K. Wang, 2007c: Significant reduction of surface solar irradiance induced by aerosols in a suburban region in northeastern China. *J. Geophys. Res.*, **112**, D22S02, <https://doi.org/10.1029/2006JD007562>.
- Xin, J. Y., and Coauthors, 2007: Aerosol optical depth (AOD) and Ångström exponent of aerosols observed by the Chinese Sun Hazemeter Network from August 2004 to September 2005. *J. Geophys. Res.*, **112**, D05203, <https://doi.org/10.1029/2006JD007075>.
- Xin, J.-Y., Q. Zhang, C.-S. Gong, Y.-S. Wang, W.-P. Du, and Y.-F. Zhao, 2014: Aerosol direct radiative forcing over Shandong Peninsula in East Asia from 2004 to 2011. *Atmos. Oceanic Sci. Lett.*, **7**, 74–79, <https://doi.org/10.3878/j.issn.1674-2834.13.0072>.
- Yang, S., G. Y. Shi, B. Wang, H. L. Yang, J. Q. Zhao, and S. G. Qin, 2011: The application of AOD's spectral curve parameter to judgment of aerosol particle size. *Journal of Applied Meteorological Science*, **22**(2), 152–157, <https://doi.org/10.3969/j.issn.1001-7313.2011.02.004>. (in Chinese)
- Yu, H., and Coauthors, 2006: A review of measurement-based assessments of the aerosol direct radiative effect and forcing. *Atmos. Chem. Phys.*, **6**, 613–666, <https://doi.org/10.5194/acp-6-613-2006>.

- Zhang, D., Y. Wang, Y. R. Feng, and Y. C. Fang, 2014: Analysis and forecasting of high-humidity weather in Guangdong in February and March. *Meteorological Science and Technology*, **42**(2), 302–308, <https://doi.org/10.3969/j.issn.1671-6345.2014.02.021>. (in Chinese)
- Zheng, M., and Coauthors, 2011: Sources of excess urban carbonaceous aerosol in the Pearl River Delta Region, China. *Atmos. Environ.*, **45**, 1175–1182, <https://doi.org/10.1016/j.atmosenv.2010.09.041>.
- Zhu, J., H. Z. Che, X. Xia, H. B. Chen, P. Goloub, and W. X. Zhang, 2014: Column-integrated aerosol optical and physical properties at a regional background atmosphere in North China Plain. *Atmos. Environ.*, **84**, 54–64, <https://doi.org/10.1016/j.atmosenv.2013.11.019>.
- Zhuang, B. L., S. Li, T. J. Wang, J. J. Deng, M. Xie, C. Q. Yin, and J. L. Zhu, 2013: Direct radiative forcing and climate effects of anthropogenic aerosols with different mixing states over China. *Atmos. Environ.*, **79**, 349–361, <https://doi.org/10.1016/j.atmosenv.2013.07.004>.